TRIBOLOGIA - Finnish Journal of Tribology 3-4 vol 42/2025

https://doi.org/10.30678/fjt.156810

SUOMEN TRIBOLOGIAYHDISTYS RY
THE FINNISH SOCIETY FOR TRIBOLOGY
www.tribologysociety.fi
https://journal.fi/tribologia

Effect of 80% diamond content on the tribological behavior of Diamond-Ti_3SiC_2 composites against various counterfaces

Liang Li[1,2*], Boke Sun[1], Zhanlong Liu[1], Jing Wei[1], Yongzhi Yu[1], Yuqi Chen[1,3]

[1]Intelligent Manufacturing and Electrical Engineering, Nanyang Normal University, Nanyang, Henan, 473061, China

[2]Jinguan Electric Co., Ltd., Nanyang, Henan, 473061, China

3Collaborative Innovation Center of Intelligent Explosion-proof Equipment, Nanyang Normal University, Nanyang, Henan, 473061, China

Corresponding author: Liang Li (liliangjdgc@nynu.edu.cn)

ABSTRACT

To meet the growing demand for wear-resistant and stable frictional materials in advanced engineering applications, polycrystalline diamond composites with 80 wt% diamond were fabricated using Ti_3SiC_2 as a ceramic binder under high pressure and high temperature. The microstructural analysis confirmed that the high diamond content ensured uniform dispersion within the matrix and strong interfacial bonding, which effectively improved composite integrity. Tribological tests against agate, polymers (POM and PP), and aluminum revealed that the composites exhibited stable friction coefficients ranging from 0.18 to 0.52 under varied loads and sliding speeds. Distinct wear mechanisms were identified depending on the counterface: abrasive wear dominated for glass, a combination of abrasive and adhesive wear occurred for polymers, while adhesive wear prevailed for metallic counterparts. Importantly, the composites showed lower friction and reduced wear at elevated loads or speeds, highlighting the stabilizing role of diamond reinforcement in the Ti_3SiC_2 matrix. These results demonstrate that introducing 80 wt% diamond markedly enhances both wear resistance and frictional stability, making such composites promising candidates for cutting, drilling, and other superhard tribological applications in demanding service environments.

Keywords: Counterface effect; Diamond–Ti_3SiC_2 composite; Friction coefficient; High-pressure sintering; Tribological behavior; Wear mechanism.

1. Introduction

Diamond composites, consisting of diamond particles and suitable binders, are widely used in cutting, drilling, and polishing applications owing to their exceptional hardness and wear resistance [1, 2]. The binder phase plays a decisive role in determining the overall mechanical and tribological performance of diamond composites [3]. Conventional metallic binders such as Co and Al offer good toughness but suffer from poor thermal stability and chemical degradation, whereas ceramic binders such as TiC or TiN provide higher stiffness but often result in brittle failure [4, 5]. To overcome these limitations, ternary carbides such as Ti_3SiC_2 have been proposed as promising alternatives due to their unique combination of metallic and ceramic characteristics, including high thermal shock resistance, electrical conductivity, machinability, and improved fracture toughness [6, 7]. These properties make Ti_3SiC_2-based composites attractive candidates for engineering applications under severe service conditions.

Previous studies have mainly focused on Ti_3SiC_2–diamond or Ti_3SiC_2–cBN composites fabricated under ultra-high pressures (7–8 GPa) [8, 9], with relatively low diamond contents of 30–50 wt% [10]. While these investigations confirmed the feasibility of using Ti_3SiC_2 as a binder, they did not fully address the influence of high diamond content on microstructural stability and tribological performance. Moreover, the effect of different counterface materials, which directly reflects the applicability of these composites in real engineering environments, has not been systematically evaluated. In particular, the stability of Ti_3SiC_2 within diamond-rich composites remains largely unexplored.

In this study, Ti_3SiC_2 bonded diamond composites with 80 wt% diamond were synthesized under high-pressure and high-temperature (HPHT) conditions. The exceptionally high diamond fraction is expected to significantly enhance the hardness and wear resistance of the composites while maintaining strong interfacial bonding through the Ti_3SiC_2 matrix. The tribological behaviour of the composites was systematically investigated against various counterface materials, including agate, polymers (POM with the glass transition temperatures in the range of -60 °C to -85 °C and PP with

Table 1 Summary of Material Physical Properties

Material	Density ($g \cdot cm^{-3}$)	Hardness (GPa)	Thermal Conductivity ($W \cdot m^{-1} \cdot K^{-1}$)
Diamond	3.52	70-100	1500
Ti_3SiC_2	4.53	4-6	~40
Agate	2.60-2.65	7-8	1.5-1.8
POM	1.41-1.42	~0.15	0.20-0.35
PP	0.90-0.91	~0.07	0.10-0.22
Al	2.70	~1.0	200-220

the glass transition temperatures in the range of -10 °C and -20 °C), and aluminium, under dry sliding conditions. By analysing the friction coefficients (abbreviated as COF), wear mechanisms, and load/speed dependencies, this work aims to clarify the role of ultra-high diamond content in improving the tribological stability of Ti_3SiC_2 composites. The results provide valuable insights into the design of next-generation superhard composites for engineering applications such as precision machining, advanced cutting tools, and wear-resistant components.

2. Materials and Methods

2.1 Synthesis of Diamond-Ti_3SiC_2 Composites

Laboratory-synthesized Ti_3SiC_2 powders (2–5 μm) were prepared using a tube furnace (XY-1600MT, Nanyang Xinyu New Materials Technology Co., Ltd., China). Commercial diamond particles (40–60 μm, AMD Diamond Powder Co., China) were selected as the reinforcement phase. The powders were weighed at a mass ratio of 1:4 (Ti_3SiC_2: diamond, corresponding to 80 wt% diamond) and mixed for 4 h using a high-efficiency mixer (KE-0.4L, Zhejang Jiechen Instrument Equipment CO., LTD., China) to ensure homogeneity. The main physical properties of all materials employed in the experiments are summarized in Table 1.

The mixed powders were loaded into a graphite mold (Φ14 mm). The sample assembly was insulated using rings and plugs made of ZrO_2-based materials. HPHT sintering was conducted in a Six-Sided Press Hydraulic Machine (Model XKY-6×1200 MN, Xianyang Superhard Materials Equipment (Group) Co., Ltd., Xianyang, Shaanxi, China) under conditions of 4.5–5.5 GPa, 800–1250 °C, and a holding time of 10–120 min. After sintering, the Diamond–Ti_3SiC_2 (Abbreviation as Dia.-TSC) compacts were naturally cooled to room temperature before demolding. It is noted that under the applied conditions of 5.5 GPa and high temperature, trace diffusion of ZrO_2 from these insulating components into the sample could occur, which was subsequently identified in the XRD analysis.

2.2 Phase and Microstructural Characterization

The crystalline phases of the composites were analysed by X-ray diffraction (XRD, D8 ADVANCE, Bruker AXS, Germany) using Cu Kα radiation (λ = 1.5406 Å). Microstructural observation of fracture surfaces and wear surfaces of Dia.-TSC was performed using scanning electron microscopy (SEM, JSM-6390LV, JEOL, Japan). The chemical composition and element distribution were further investigated by energy dispersive spectroscopy (EDS, INCA-ENERGY 250, Oxford Instruments, UK). Three sintering conditions (5 GPa, 5.5 GPa, and 5.5 GPa/1100 °C) were applied to study the microstructural evolution of the Dia.-TSC composites. For all subsequent tribological tests, only the composite sintered at 5.5 GPa and 1100 °C (shown in Fig. 2c) was used, as it exhibited the highest densification and most homogeneous microstructure.

2.3 Friction and Wear Tests

The tribological properties of the Dia.-TSC composites were evaluated using a ball-on-disk configuration on a reciprocating tribometer (CFT-I, Zhongke Kaihua Instrument Equipment Co., China) in ambient air without lubrication. Composite specimens were mounted on the disk, while Φ4 mm balls of different counterface materials (agate, polyoxymethylene (POM), polypropylene (PP), and aluminum) served as the pins. All synthesized diamond composites were uniformly surface-treated with a diamond grinding wheel after sintering to ensure similar surface roughness at the initial stage of the experiments. The commercially spheres possess comparable surface roughness.

In this setup, a stationary (agate/POM/PP/Al) ball was loaded against the surface of the rotating composite disk sample. A linear reciprocating motion was applied to the disk (or the ball holder), with a fixed stroke length of 5 mm. The tribological tests were carried out under applied loads of 5–12 N, reciprocating frequencies of 300 -600 R/min (converted to average sliding velocities). Each test was a continuous run; the reciprocating motion did not involve pauses at the turning points. The COF was recorded in situ

throughout the entire test duration, typically set to 30 min. The PV value (the product of load pressure P and sliding velocity V) serves as a key parameter for assessing the intensity of frictional heat generation in sliding contacts. To assess the potential influence of frictional heating under different test conditions, a theoretical estimation of the contact ("flash") temperature was performed for the most severe operating parameters (12 N, 0.1 m/s). The estimation was based on the classical Jaeger moving heat source model, using the formula $\Delta T \approx \mu \cdot F_N \cdot v/(4 \cdot a \cdot k_{eff})$. The key input parameters were: the measured average COF (μ) for each material pair, the applied normal load (F_N), the calculated average sliding velocity (v), the Hertzian contact radius (a), and an equivalent thermal conductivity (k_{eff}). The value of k_{eff} was calculated considering heat conduction into both contacting bodies ($k_{eff} = 2k_1k_2/(k_1 + k_2)$). The purpose of this estimation was to provide a qualitative understanding of the thermal regime, particularly to distinguish between conditions where frictional heat is readily dissipated (e.g., against high-conductivity Al) or likely to accumulate (e.g., against low-conductivity polymers). The implications of these estimations for interpreting the wear mechanisms are discussed in Section 3 (Results and Discussion).

After testing, the wear tracks on both the composite specimens and counterface balls were examined. The wear loss was calculated by measuring the mass loss of the composite material and the counterpart ball before and after the friction test, using an electronic balance with an accuracy of 0.1 mg (1/100,000). The worn surfaces were characterized by optical microscopy (Axio Imager, High-Temperature Metallographic Microscope, Carl Zeiss Microscopy GmbH, Jena, Germany) and surface profilometry (Nanovea PS50, Nanovea Inc., Irvine, CA, USA) to determine track geometry. To distinguish the dominant wear mechanisms (adhesive versus abrasive wear) in the subsequent analysis, a qualitative assessment of the wear scar morphology on the counterpart balls was conducted, based on the classical tribological model that considers total wear as the sum of adhesive and abrasive components. Detailed surface morphology and wear mechanisms were further analysed using SEM/EDS.

3. Results

3.1 XRD results of Diamond-Ti_3SiC_2 composites

Figure 1 shows the XRD results of raw Ti_3SiC_2 and Diamond powder after sintering at 3- 5 GPa and 900 -1250 °C. Based on the XRD results, Ti_3SiC_2 remains stable after sintering with diamond at 3 GPa and 800°C and at 4.5 GPa and 950°C, with no Ti alloy or carbide peaks detected. However, TiC impurity peaks appear at 5 GPa and 1050° C., Ti_3SiC_2 peaks nearly disappear at 1250 °C, and TiC-diamond composite formed. Minor ZrO_2 contamination, identified via XRD, is attributed to the high-pressure cell assembly. Under the extreme conditions of 5.5 GPa and elevated temperature, ZrO_2 from the insulating rings and isolation plugs surrounding the sample can diffuse into the compact.

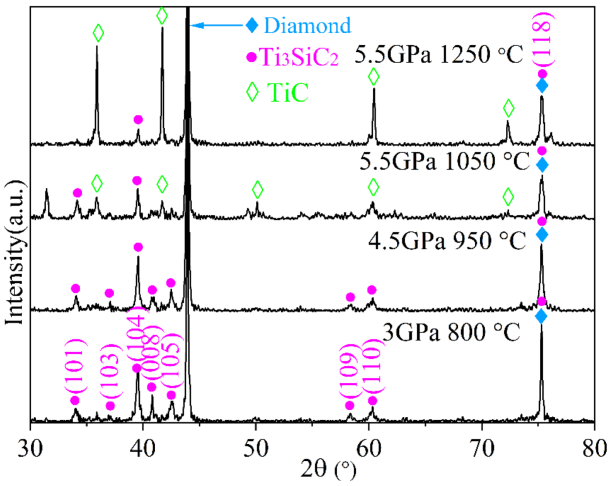

Figure 1. XRD patterns of Dia.-TSC under 4.5 – 5.5 GPa at 800 – 1250 °C.

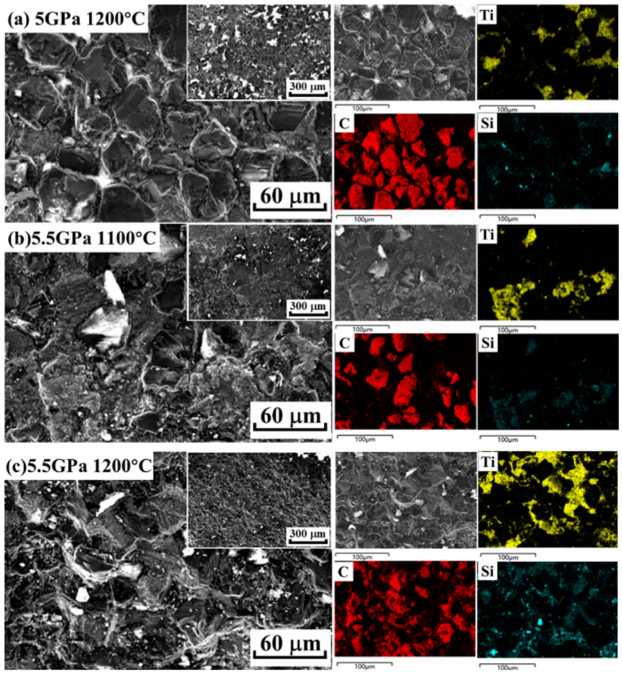

Figure 2. SEM images and EDS mappings of Dia.-TSC composites sintered: at (a) 5 GPa and 1200 °C; (b) 5.5 GPa and 1100 °C; (c) 5.5 GPa and 1200 °C.

3.2 Microstructure of Diamond-Ti_3SiC_2 composites

Figure 2 presents the SEM morphologies and EDS mappings of Dia.-TSC composites sintered under different conditions. At 5 GPa (Fig. 2a), diamond grains are uniformly distributed in the Ti_3SiC_2 matrix with tight interfacial bonding and no obvious microcracks. With increasing pressure to 5.5 GPa (Fig. 2b), Dia.-TSC composites show improved densification, but local diamond fracture and slight agglomeration appear. At higher temperature under 5.5 GPa (Fig. 2c), the structure becomes denser, and diamond dispersion is more homogeneous. EDS confirms that Ti and Si are mainly

concentrated in the matrix, while C is enriched in the diamond phase, indicating effective encapsulation of diamond by the binder. Based on its superior densification and interfacial integrity, this sample (5.5 GPa/1100 °C) was selected for all subsequent wear evaluations.

3.3 Friction properties of Diamond-Ti_3SiC_2 composites sintered by HPHT

3.3.1 Agate

The tribological properties of the Dia.-TSC composite sintered at 5.5 GPa and 1100 °C (see Fig. 2c) were evaluated under dry sliding conditions against various counterpart materials. Figure 3a shows the COF of Dia.-TSC composite and agate with time. It is noteworthy that the COF decreased from an average of around 0.22 at 300 R/min to a minimum of 0.12 at 600 R/min under load 9.8 N. This negative correlation between rotational speed and COF can be attributed to the formation and stability of a tribo-film at higher speeds. As the rotational speed increases, the frictional contact frequency rises, potentially leading to a localized temperature increase at the asperity level. This thermal energy may facilitate the oxidation of Ti_3SiC_2 or the graphitization of the diamond phase, resulting in the in -situ formation of a low-shear-strength tribo-layer (e.g., graphite or titanium oxides) on the contact surface (Fig. 4c). This layer acts as a solid lubricant, effectively reducing the COF. The referenced Ti_2AlC–TiC and Ti_3AlC_2–TiC composites, with a COF ranging from 0.5 to 1.2, are significantly higher[11] . This stark contrast highlights the superior lubricating capability provided by the diamond phase and the specific tribo-chemistry of Ti_3SiC_2. This synergy arises from the combination of the intrinsically low shear strength of diamond and the formation of a shear-prone oxide film derived from Ti_3SiC_2 tribo-oxidation.

The mass loss of Dia.-TSC discs ranged from 0.4 to 9.6 mg. The maximum mass loss of the Dia.-TSC disc at 300 R/min, attributed to abrasive wear, suggests that at lower speeds, the contact is characterized by plowing and micro-cutting by hard counter-face asperities or debris (Fig. 5a and Fig. 6a). As the speed increases to 600 R/min, the wear mechanism likely shifts towards milder adhesive or surface fatigue wear, facilitated by the protective tribo-film (Fig. 5d and Fig. 6d).

With increasing rotational speed, the mass loss of the agate counterpart exhibited a decreasing trend, varying from 0.2 to 2.5 mg and reaching its minimum at the highest speed. At elevated speeds, a lubricating tribo-film may have formed on the surface of the composite, which not only reduced the COF but also mitigated abrasive wear on the agate ball, thereby lowering its wear loss. Consequently, the Dia.-TSC composite achieved favorable low-friction and low-wear characteristics for both counterparts at 600 R/min, representing a highly valuable advantage for engineering systems that demand long service life and stable operation.

At a rotational speed of 600 R/min, the effect of load on

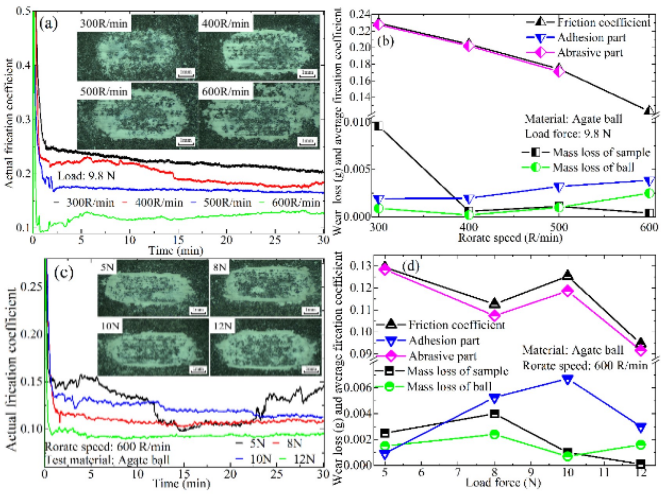

Figure 3. COF (a) and weight loss (b) of Dia.-TSC composite with agate pair under 9.8 N at 300–600 R/min; COF (c) and weight loss (d) of the synthetics under 5–12 N at 600 R/min.

the COF between Dia.-TSC composite and agate is discussed. The COF of Dia.-TSC composites with agate friction pair is between 0.1 and 0.15. The initial decrease in the COF at a low load of 5 N is typical of a "run-in" period, where surface asperities are gradually worn down, leading to improved conformity and the initial formation of a lubricating tribo-film. The subsequent increase suggests that this film may be unstable or insufficient at very low contact pressures, leading to periodic direct contact and mild adhesive wear.

The non-monotonic trend in the 8-12 N range—where the COF first increases and then decreases with load—is particularly significant. The increase in COF at 10 N, attributed to the adhesive wear effect, indicates a transitional regime. At this critical load, the contact pressure might be high enough to cause localized micro-welding and material transfer (adhesion), but not yet sufficient to consistently promote the formation of a robust, low-shear-strength tribo-film. As the load increases further, the PV value (contact pressure × sliding velocity) rises, potentially facilitating the accelerated formation of a more continuous and stable lubricious layer, possibly through enhanced graphitization of diamond or oxidation of the Ti_3SiC_2 phase. This leads to the subsequent decrease in COF, marking a shift in the dominant wear mechanism from a mix of abrasion and adhesion back to a more controlled abrasive wear governed by the protective film. The mass loss of Dia.-TSC discs ranged from 0.1 to 4 mg, while that of the agate balls ranged from 0.7 to 2.4 mg. The abrasive wear effect gradually increased with increasing load, and the component of adhesive wear weakened (Fig. 3d).

Figure 4a shows the SEM micrograph of the wear scar on the Dia.-TSC composite after sliding against an agate counterface. The worn surface exhibits crater-like features generated during reciprocating motion; however, the diamond particles remain well anchored within the Ti_3SiC_2

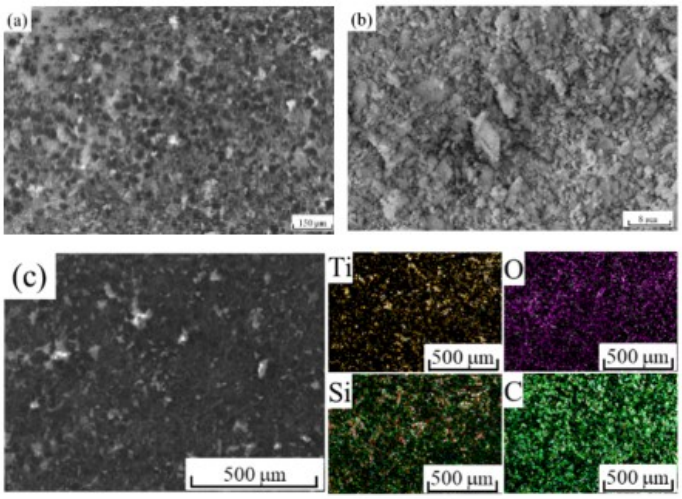

Figure 4. SEM images of abrasion marks on the sample surface (a), localized enlargement of abrasive chips (b), and EDS map analysis of abraded surfaces (c).

matrix, without evidence of extensive pull-out, demonstrating the high interfacial bonding strength between the reinforcing and binder phases. The corresponding agate-derived debris displays irregular morphologies and is found to adhere locally to the composite surface, suggesting a cold-welding–like deposition mechanism (Fig. 4b). Figure 4c presents the EDS elemental distribution of a representative wear scar region. The results indicate that the adhered debris consists predominantly of silica (SiO_2), which preferentially accumulates in the vicinity of diamond grains. Concurrently, oxidation of the Ti_3SiC_2 binder phase was detected, leading to the in-situ formation of a tribo-oxide film primarily composed of SiO_2 and TiO_2. This protective tribo-film is considered to play a significant role in reducing friction and mitigating wear during sliding against agate.

SEM images of the composite wear tracks (Fig. 5) reveal a clear dependence of wear mechanisms on sliding speed and applied load. At low speed (300 R/min), coarse, flaky debris and adhesive junctions dominate, producing unstable friction and severe material loss. In contrast, at higher speed (600 R/min), fine debris and a continuous tribo-film indicate a transition toward a more ductile, less destructive wear mode, accompanied by stabilized friction and reduced wear.

Load variation exerts a similar influence. At 5 N, wear remains mild with smooth tracks, while higher loads (10–12 N) generate dense fine debris and localized craters, highlighting intensified abrasive–adhesive interactions. This agrees with the non-monotonic friction response, where the balance between competing wear modes becomes critical.

The combination of a low COF (0.12) and low mass loss of the diamond phase at 600 R/min under a 9.8 N load positions the Dia.-TSC composite as an excellent candidate for high-speed, light-to-medium load tribological applications. While graphite/MoS_2-based composites

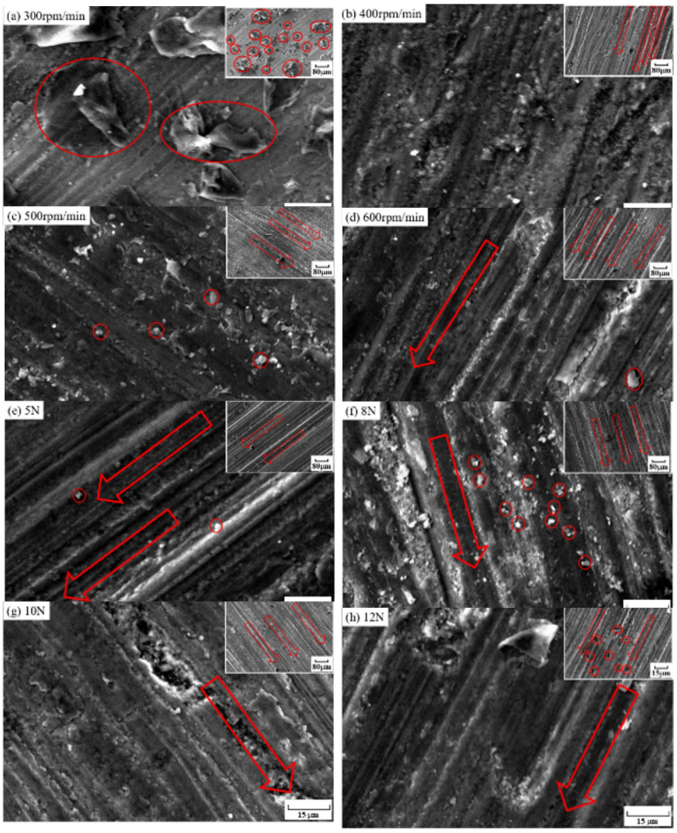

Figure 5. SEM image of wear track of agate ball under 9.8 N at 300 R/min (a); 400 R/min (b); 500 R/min (c); 600 R/min (d); under 5 N (e); 8 N (f); 10 N (g); 12 N (h) at 400 R/min.

exhibit very low COF (<0.1) in certain environments [12], their operational temperature and humidity limits are restrictive. Dia.-TSC composite likely offers better performance stability in humid or elevated temperature conditions. Structural ceramics (e.g., Al_2O_3, AlN) are wear-resistant but often exhibit higher COF [13]. Dia.-TSC composite provides a unique combination of the hardness and wear resistance of diamond with the lubricity of MAX phases. Therefore, the Dia.-TSC composite achieve a balance of low friction, high wear resistance, and potential environmental adaptability, which is of great significance for the grinding and processing of agate materials.

3.3.2 POM

Figure 6a shows that the COF of Dia.-TSC composites with POM pair decreases initially and then increases as sliding speed rises from 300 to 600 R/min under a 9.8 N load. The Dia.-TSC (blue curve) consistently exhibits lower and more stable COF values (~0.28 at 600 R/min) compared to the binder-rich Diamond–$Ti_3Si_{0.8}Al_{0.2}C_2$ composite (TSAC-D, 60 wt% diamond, dotted curve) [14].

This trend can be understood in terms of contact mechanics, third-body dynamics, and tribo-film formation. The higher hardness and stiffness of the diamond-rich composite reduce the real contact area, thereby limiting adhesive junctions with the polymer counterface and stabilizing friction at a lower plateau [15]. At low speed (300 R/min), coarse debris and strong adhesive

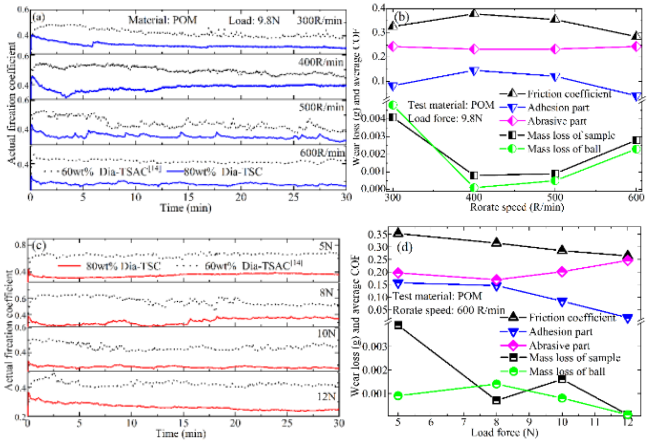

Figure 6. COF (a) and weight loss (b) of the synthetics with POM pair under 9.8 N at 300–600 R/min; COF (c) and weight loss (d) of the synthetics under 5–12 N at 600 R/min.

interactions dominate, producing high and fluctuating COF. With increasing speed, the debris is refined into finer particles, which act as a load-carrying third body that smooths shear processes and reduces adhesion. This effect is especially pronounced in the 80 wt% diamond composites, where diamond fragments are less prone to severe pull-out [16].

Frictional heating at higher speeds further contributes by accelerating tribochemical reactions and facilitating the formation of lubricious oxide or amorphous films [17]. These tribo-films reduce interfacial shear strength and stabilize COF. The more uniformly distributed binder matrix in Dia.-TSC promotes the development of continuous tribo-films, in contrast to the patchy adhesive transfer often observed in Diamond–$Ti_3Si_{0.8}Al_{0.2}C_2$ [14].

The wear data corroborates these mechanisms. At 300 R/min, Dia.-TSC composites exhibit the highest mass loss (≈4.1 mg), dominated by adhesive wear as exposed diamond asperities plough into the softer POM and detach matrix fragments. As speed increases to 400–500 R/min, composite wear decreases significantly while POM wear first decreases and then increases. This transition corresponds to the formation of a continuous POM transfer film, which functions as a solid lubricant and promotes a mutually beneficial tribological state characterized by low friction (≈0.1–0.3) and reduced wear for both counterparts. At 600 R/min, however, excessive heating destabilizes this transfer film, reactivating abrasive processes and accelerating POM degradation.

From an engineering standpoint, these results identify an optimal operating window (400–500 R/min), where the self-lubricating transfer film ensures simultaneously low friction and low wear on both contacting surfaces. Compared with traditional hard–hard contacts (e.g., agate), this composite–polymer pairing achieves markedly lower COF, well below values reported for diamond-based composites against ceramics [13]. This highlights the potential of Dia.-TSC composites for precision, lightweight,

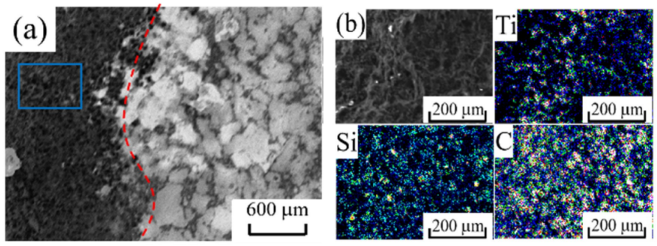

Figure 7. SEM image of wear track of Dia.-TSC composites with counterface of POM (a); EDS image of black area (b).

and high-speed systems, provided that operating conditions and thermal management are carefully controlled.

The COF of Dia.-TSC composites decreases with increasing load at 600 R/min (Fig. 6c). The COF reaches a minimum value of 0.26 at a load of 12 N. The effect of abrasive wear gradually increases with increasing load and the component of adhesive wear decreases. The mass loss of Diamond–Ti_3SiC_2 discs and POM balls was 0.1 - 3.9 mg and 0. 1- 1.4 mg, respectively (Fig. 6d).Figure 7 shows the typical wear morphology of the Dia.-TSC composite after sliding against a POM ball. The sample surface can be clearly divided into friction-affected zones (dark areas) and debris-covered areas (light areas). In the friction-affected zones, continuously distributed black wear debris is observed to be predominantly accumulated along grain boundaries, with occasional debris also found within the grain interiors. This specific distribution suggests that stress concentration preferentially occurs at the grain boundaries during the friction process, leading to the fragmentation and detachment of grain boundary material, thereby forming wear debris. The material removal during the sliding contact between the Dia.-TSC composite and the POM counterpart is primarily achieved through a combination of stable abrasive wear and initial adhesive wear.

The morphology of wear scars on POM balls evolves significantly with increasing rotational speed from 300 to 600 R/min as shown in Figures 8a-d. At lower speeds (300 R/min, Fig. 8a), the wear scar exhibits clear boundaries and contains fine granular debris within the pits. With increasing rotational speed, the wear scar boundaries become progressively blurred. Notably, the debris morphology transitions from fine granular particles (Fig. 8a) to flaky particles (Fig. 8d), indicating a gradual shift in the dominant wear mechanism from abrasive wear to adhesive wear. This transition can be attributed to the accumulation and insufficient discharge of wear debris under high-speed conditions, where these particles function as third-body abrasives during friction. The plastic deformation induced by these debris particles exacerbates sub-surface wear, consequently leading to an elevated COF as observed in Fig. 6b.

Figures 8e-h present the SEM images of POM ball wear tracks under varying loads (5-12 N) at a constant rotational speed of 400 R/min. Low-magnification observations reveal that the wear surface primarily consists of shallow

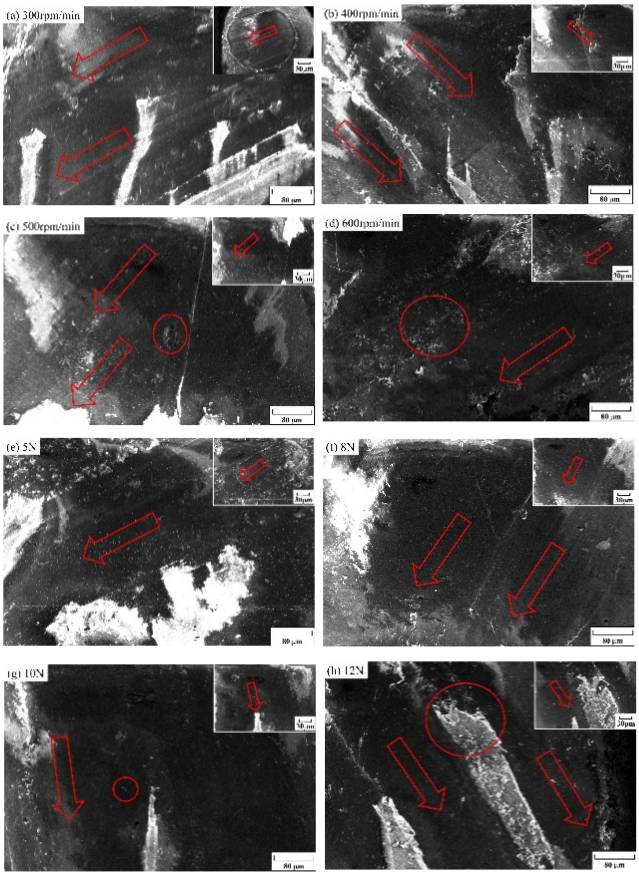

Figure 8. SEM image of wear track of POM ball under 9.8 N at 300 R/min (a); 400 R/min (b); 500 R/min (c); 600 R/min (d); under 5 N (e); 8 N (f); 10 N (g); 12 N (h) at 400 R/min.

grooves. As the normal load increases, a gradual generation of flaky abrasive debris becomes apparent on the wear surface. This morphological evolution demonstrates the load-dependent nature of wear mechanisms in the POM ball counterpart, with increasing adhesion components contributing to material removal at higher contact pressures.

Figure 9 presents the 3D topography of wear tracks on POM balls under different testing conditions. Under a constant load of 9.8 N (Figs. 9a-d), the wear track morphology shows significant evolution with increasing rotational speed. The track width increases progressively while the surface roughness within the track undergoes noticeable changes, transitioning from relatively smooth features to more pronounced plastic deformation characteristics. This morphological transition corresponds well with the observed shift in wear mechanisms from abrasive to adhesive dominance in SEM observations, while also providing three-dimensional evidence for the trend of initially decreasing and then increasing COF.

Under constant rotational speed of 400 R/min with varying loads (Figs. 9e-h), the wear tracks demonstrate clear load-dependent characteristics. As the normal load increases from 5 N to 12 N, both the width and depth of the tracks show progressive enlargement. The 3D topography reveals enhanced plastic deformation and

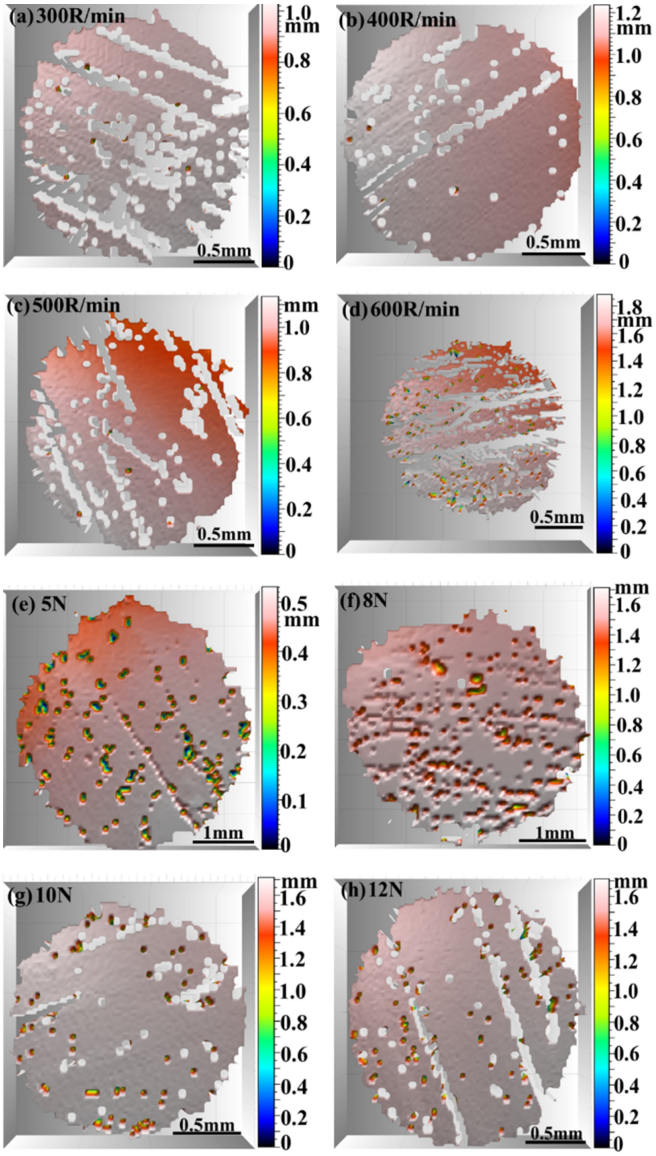

Figure 9. 3D surface topographies of wear track of POM ball under 9.8 N at 300 R/min (a); 400 R/min (b); 500 R/min (c); 600 R/min (d); under 5 N (e); 8 N (f); 10 N (g); 12 N (h) at 400R/min.

material accumulation at the track edges under higher loads. These 3D morphological features effectively corroborate the SEM observations of flake-like debris generation and the non-monotonic variation in COF with increasing load, providing comprehensive understanding of the load-dependent wear behavior in the POM/Dia.-TSC tribological system.

3.3.3 PP

Figure 10(a–b) shows that the COF of Dia.-TSC composites sliding against PP is high but narrowly distributed (≈0.47–0.53) and that two clear trends emerge: (i) at 500–600 R/min the COF decreases sharply after an extended run-in (>15 min), attaining a minimum mean value of ≈0.473 at 600 R/min; (ii) at a fixed speed (600 R/min) COF falls with increasing normal load, reaching a

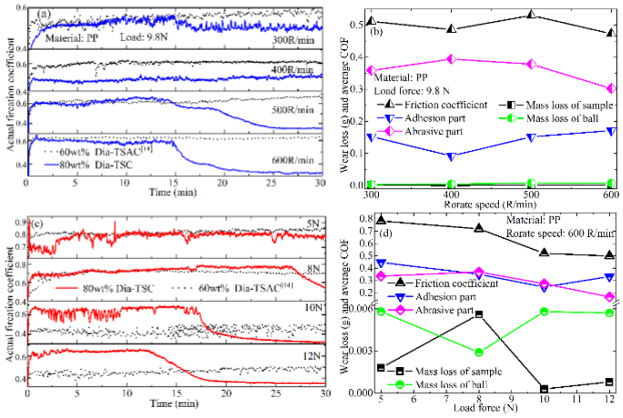

Figure 10. COF (a) and weight loss (b) of the synthetics with PP pair under 9.8 N at 300–600 R/min; COF (c) and weight loss (d) of the synthetics under 5–12 N at 600 R/min.

minimum near 0.50 at 12 N while the COF range widens at lower loads (0.50–0.78 across the tested range).

These observations can be rationalized by third-body evolution, interfacial thermal effects and load-dependent film mechanics. At low speeds the contact remains in an abrasive/adhesive regime with limited polymer transfer and coarse third-body debris; this produces relatively high and unstable COF. At higher sliding speeds (≥500 R/min) frictional heating promotes polymer softening and encourages the formation of a continuous PP transfer film or thermally activated tribo-film on the composite surface. The emergent film acts as a shearable, load-bearing third body with lower interfacial shear strength, which explains the time-dependent COF drop after the run-in period. Thermal/tribochemical reactions (oxidation, formation of low-shear organics or amorphous carbon) may further stabilize the film and reduce friction; these effects are consistent with reported polymer–hard composite behaviour [18]. Increasing normal load at a fixed high speed tends to compact and densify the transfer/third-body layer, reducing asperity contact pressure per unit area in the load-bearing film and, hence lowering the macroscopic COF. At the same time, higher contact pressure accelerates removal of weak asperities and promotes a more stable, abrasion-dominated steady state once the film is established. However, excessive load may eventually damage the film or promote particle embedding and three-body abrasion; this load window dependence is a common feature in polymer–ceramic tribo-pairs [13].

The measured COF values (≈0.47–0.53 baseline, dropping to ≈0.47 at optimal conditions) are comparable to typical PP versus hard-surface values reported in the literature (commonly 0.4–0.7, depending on surface finish and temperature) and are lower than many MAX-phase/metallic counterface pairings under similar conditions [19]. The Dia.-TSC system differs from TSAC-D [14] counterpart in that the higher diamond fraction and thinner binder channels in Dia.-TSC favor faster formation of a load-supporting tribo-film and reduce adhesive contact, thus explaining the systematically lower and more stable COF.

The wear and friction behavior of the Dia.-TSC/PP tribo-pair as a function of sliding speed and load is summarized in Fig. 10(b,d). The composite's mass loss ranged from 0 to 0.022 g, while the PP balls displayed a progressive increase in wear with higher rotational speed. The COF remained in the range 0.47–0.53, with peak stability at 600 R/min under 9.8 N.

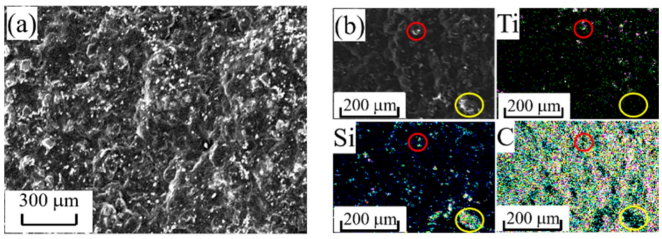

Figure 11. SEM image of wear track of Dia.-TSC composites with counterface of PP (a); EDS image of wear track (b).

At low speeds (300–400 R/min), adhesive wear dominates: coarse debris and strong adhesive junctions result in unstable friction and higher composite wear, as diamond asperities plough into the softer POM and detach binder fragments. When speed increases to 500–600 R/min, frictional heating softens or partially melts the PP surface, promoting the formation of a continuous transfer film, which acts as a lubricious third body and mitigates both adhesive and abrasive damage. Under these conditions, the composite exhibits minimal wear, while the PP counterface also benefits. This mechanism aligns with the established role of polymer transfer films in reducing wear by shielding direct contact and smoothing shear [20, 21].

Figure 10(d) also reveals that at 600 R/min, increasing load from 5 to 12 N compresses the transfer film and enhances its load-carrying capacity, reducing COF and composite wear down to a minimum (~0.3–5.6 mg). Above an optimal load (~10 N), the film may degrade locally under high stress, and abrasive wear starts to reemerge. This load-dependent behaviour of polymer–ceramic contacts is consistent with insights from polymer tribology literature [22].

Figure 11 shows SEM image of wear surfaces of Dia.-TSC composite in the load of 9.8 N at the sliding speed of 300 R/min with counterface of PP. Similar to POM, many grinding pits were observed after diamond grains peeled off. Because of the uniform distribution of pits and no deformation, the wear process is more regular, and the wear mechanism should mainly be fatigue wear. In addition, there are a lot of dispersed granular wear debris on the friction surface. Based on EDS results in red and yellow circular frames (Fig. 10b), the wear debris is Ti_3SiC_2 and Si matrix phases. It is inferred that there is some abrasive wear when PP is used as friction pair.

Figure 12a-d shows the surface wear marks of PP balls at wear rates of 300-600 R/min under 9.8N. With the increase of friction rate, the edge of the wear scar changes from an irregular arc to a regular line, and the number of wear particles at the edge of the wear scar also increases. The friction mechanism changes from fatigue wear to abrasive wear with the increase of friction rate.

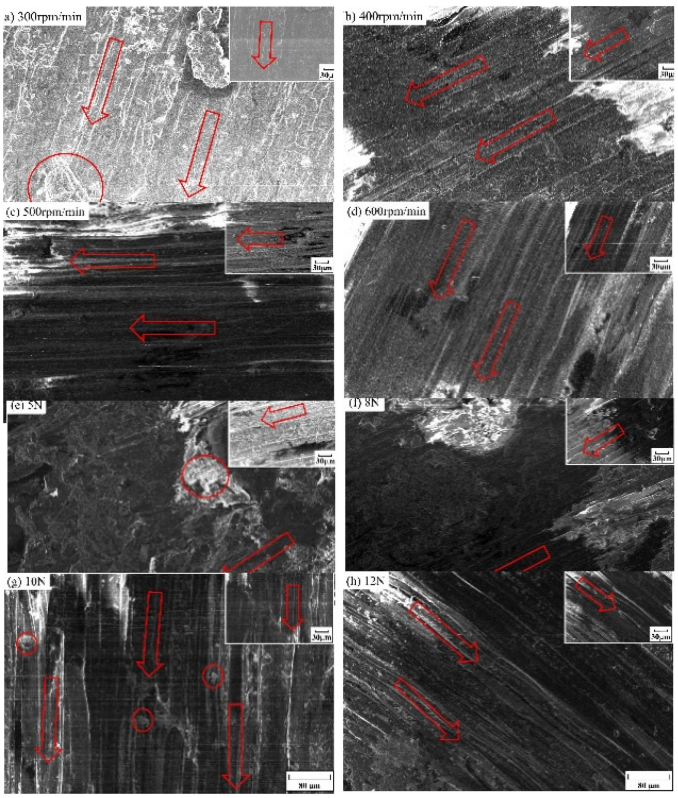

Figure 12. SEM image of wear track of PP ball under 9.8 N at 300 R/min (a); 400 R/min (b); 500 R/min (c); 600 R/min (d); under 5 N (e); 8 N (f); 10 N (g); 12 N (h) at 400 R/min.

Figure 12e-h shows the surface abrasion marks of PP balls under 5-12 N at 400 R/min. With the increase of pressure, the shape of the abrasion mark remains linear, but the depth of the abrasion mark increases gradually. This is because higher pressures cause closer contact between the friction surfaces, increasing the likelihood of hard particles (such as diamond particles in the matrix) embedding and scratching, resulting in an increase in the depth of the abrasions.

Figure 13 presents the 3D topography of the wear tracks formed on PP balls under various loads and rotational speeds. Under a constant load of 9.8 N (Figs. 13e–h), the wear morphology evolves distinctly with increasing speed. At 300 R/min, the wear track appears relatively shallow but uneven, with scattered furrows indicating localized ploughing and adhesive tearing. As the speed rises to 400 R/min, the surface becomes smoother, and the furrows exhibit reduced depth, suggesting the onset of a mild adhesive regime accompanied by partial formation of a transfer layer. At 500 R/min, the track displays a more homogeneous texture with aligned micro-grooves, consistent with stable sliding and balanced third-body formation. When the speed reaches 600 R/min, the wear track width slightly increases again, and deeper grooves reappear, implying that excessive frictional heating has led to softening or local thermal degradation of the PP surface, weakening the transfer film and re-enhancing abrasive action.

When the rotational speed is fixed at 400 R/min (Figs. 13a–d), the influence of load on wear morphology becomes evident. At 5 N, shallow grooves dominate the wear scar, while at 8 N, the track deepens and exhibits clear signs of plastic flow and material accumulation at the edges. The 10 N sample shows the smoothest wear morphology with moderate furrows and minimal debris adhesion, correlating with the lowest measured wear rate. As the load further increases to 12 N, severe deformation bands and large agglomerated debris are observed, indicating the transition toward mixed abrasive–adhesive wear.

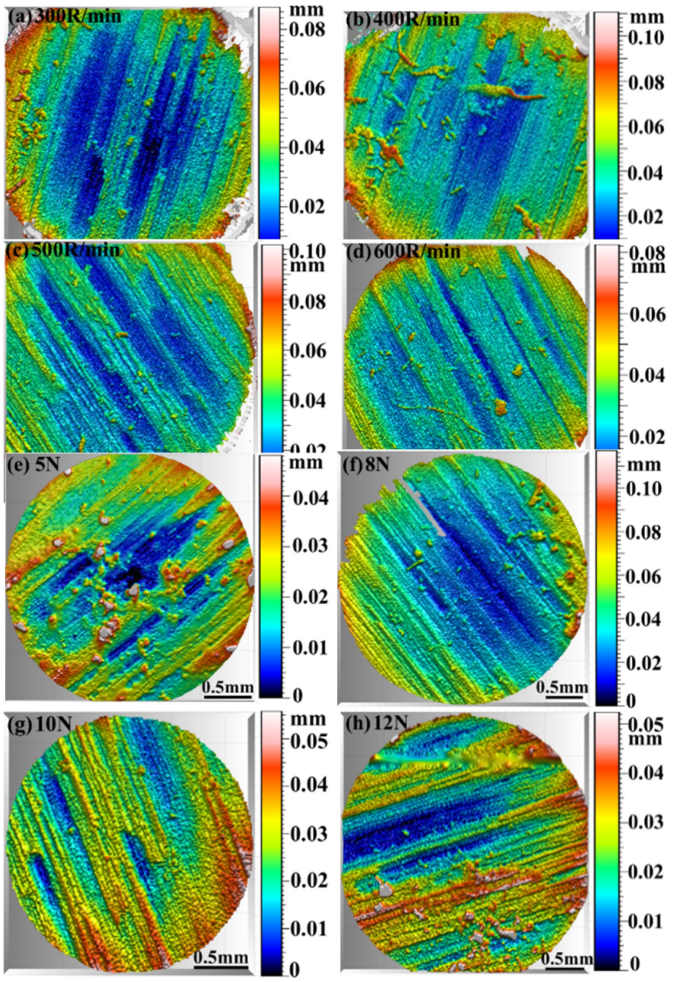

Figure 13. 3D image of wear track of PP ball under 9.8 N at 300 R/min (a); 400 R/min (b); 500 R/min (c); 600 R/min (d); under 5 N (e); 8 N (f); 10 N (g); 12 N (h) at 400 R/min.

These 3D surface profiles quantitatively illustrate the transition of wear mechanisms with both load and sliding speed. The observed evolution—from mild abrasive wear at low load/speed to transfer-film-controlled mild wear at intermediate conditions, and then to thermally assisted deformation at higher parameters—aligns with the wear trends shown in Figs. 13(b,d). The results highlight the critical role of maintaining an optimal thermo-mechanical balance at the PP/Diamond–Ti_3SiC_2 interface to achieve minimal wear under practical engineering conditions.

3.3.4 Al

Figure 14a illustrates the variations in the COF and

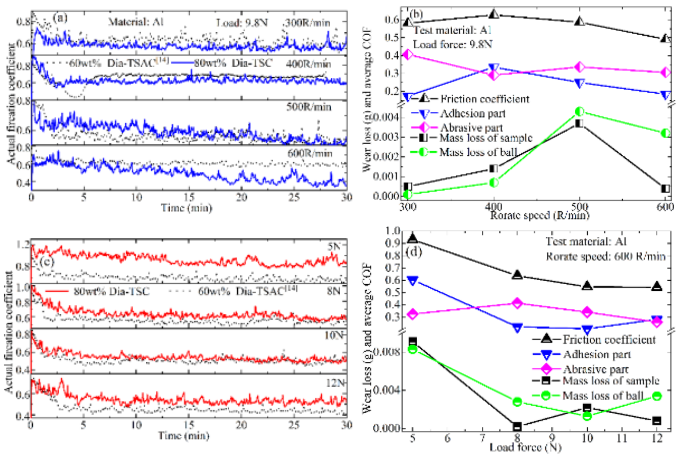

Figure 14. COF (a) and weight loss (b) of Dia.-TSC with Al pair under 9.8 N at 300–600 R/min; COF (c) and weight loss (d) of Dia.-TSC under 5–12 N at 600 R/min.

wear losses of Dia.-TSC composites sliding against Al counterparts under different rotational speeds. Under a constant load of 9.8 N, the COF first increases and then decreases with rising speed, showing a maximum value of 0.62 at 400 R/min and an overall range between 0.49 and 0.62. This non-monotonic behavior indicates the competing effects of surface oxidation, adhesive transfer, and the gradual stabilization of the contact interface. The mass loss of the composite specimens ranged from 0.4 to 3.7 mg, while that of the Al balls varied between 0.1 and 4.3 mg. The mass loss of the Al balls initially increased with speed due to enhanced adhesion and microcutting but decreased beyond 400 R/min as the formation of a transfer film and surface smoothing reduced further wear.

Figure 14c presents the influence of normal load on COF and wear at a constant speed of 600 R/min. With increasing load from 5 to 12 N, the COF of Dia.-TSC/Al pair gradually decreases from 0.93 to 0.54, suggesting that the increase in real contact area and the formation of metallic transfer films promote a more stable sliding regime. The wear loss of the composites remains relatively low, owing to the protective effect of adhered Al debris, whereas the Al balls show a wear loss between 1.3 and 8.3 mg. The wear mechanism transitions from initial abrasive and ploughing wear at low loads to dominant adhesive wear accompanied by mild plastic deformation at higher loads.

Overall, the tribological behavior of Dia.-TSC composites against Al counterparts is governed by the interplay between adhesion and oxidation-induced transfer films. Compared with the POM and PP counterparts, the Al pair exhibits a higher COF but moderate wear resistance, indicating a strong adhesion tendency and metallurgical compatibility at the contact interface.

Figure 15a presents the SEM morphology of the worn surface of the Dia.-TSC composite after sliding against Al balls. The surface exhibits a distinct adhesive wear feature, where fine wear debris originating from the Al balls

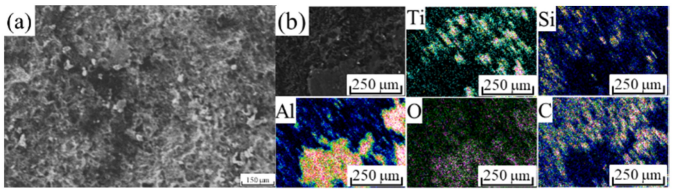

Figure 15. SEM image of wear track of Dia.-TSC composites with counterface of PP (a); EDS image of wear track (b).

strongly adheres to the composite surface. These adhered particles coalesce into flake-like layers that partially encapsulate the exposed diamond grains, indicating an adhesive transfer process between the Al counterface and the composite. The presence of these metallic flakes suggests that the soft Al material was plastically deformed and smeared over the harder composite surface during sliding, contributing to the formation of a mechanically mixed layer.

As shown in Fig. 15b, the EDS elemental mapping of the worn region reveals strong signals of Al and O, confirming that the transferred material consists primarily of oxidized aluminum. This indicates that frictional heating during sliding promoted surface oxidation of the Al ball, leading to the generation of an Al_2O_3-rich tribolayer. The coexistence of metallic Al and its oxides within this layer contributes to both the adhesive bonding and the partial lubrication effect observed in the friction process. These results further corroborate the observed transition from abrasive to adhesive wear mechanisms in the Dia.-TSC/Al tribosystem.

Figures 16a–d present the SEM morphologies of the wear track of Al balls after sliding against Dia.-TSC composites under different rotational speeds. At 300 and 400 R/min, the surfaces exhibit numerous shallow grooves, adhesive craters, and compacted debris clusters—typical characteristics of adhesive wear in metallic materials. These raised pear-shaped grooves and crater-like features indicate localized adhesion and plastic deformation of the Al surface. As the rotational speed increases to 500 and 600 R/min, both the density and size of the abrasive craters increase markedly, consistent with the enhanced material removal and wear volume shown in Fig. 16b. The morphological evolution of the wear tracks and debris confirms a transition toward more severe plowing and cutting wear modes with increasing sliding speed.

Figures 16e–h shows the worn surface morphologies of Al balls under varying loads (5–12 N). As the load increases, the grooves become deeper and more continuous, while the amount of elongated debris accumulated along the groove edges also increases. These strip-like wear chips are characteristic of cutting wear, caused by the hard diamond particles in the composite plowing into the softer Al surface. At the optimal load of 10 N (Fig. 16g), the wear debris becomes finer and more irregular, with a noticeable reduction in large flake-like fragments. This morphological refinement indicates that an appropriate increase in normal load can suppress large-area adhesive transfer, promoting a more stable mixed

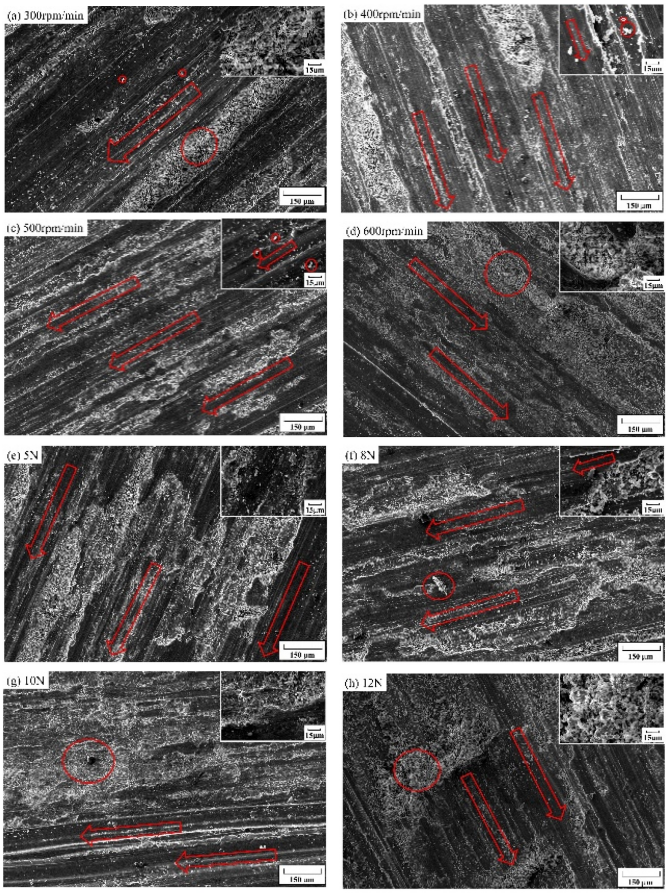

Figure 16. SEM image of wear track of Al ball under 9.8 N at 300 R/min (a); 400 R/min (b); 500 R/min (c); 600 R/min (d); under 5 N (e); 8 N (f); 10 N (g); 12 N (h) at 400 R/min.

wear regime with improved wear resistance. Overall, the observed surface features support a transition from dominant adhesive wear to combined plowing–cutting wear mechanisms as both speed and load increase.

Figure 17 presents the 3D topography of wear tracks on Al balls under varying test conditions. Under a constant load of 9.8 N (Figs. 17a–d), the wear track morphology exhibits clear evolution with increasing rotational speed. The width and depth of the tracks show progressive enlargement, accompanied by a transition in surface morphology from relatively uniform grooves to more pronounced plastic deformation and material pile-up at the edges. This transition aligns with the shift in wear mechanisms observed via SEM and supports the variation trend of the COF under increasing speed.

At a constant rotational speed of 400 R/min under different loads (Figs. 17e–h), the wear tracks display significant load-dependent morphological changes. As the load increases from 5 N to 12 N, both the width and depth of the tracks expand noticeably, with more severe surface plastic flow and material accumulation along the track boundaries. These 3D features provide clear evidence for the transition in wear mechanisms and help explain the variation in friction behavior with load within the Al-based tribo-system.

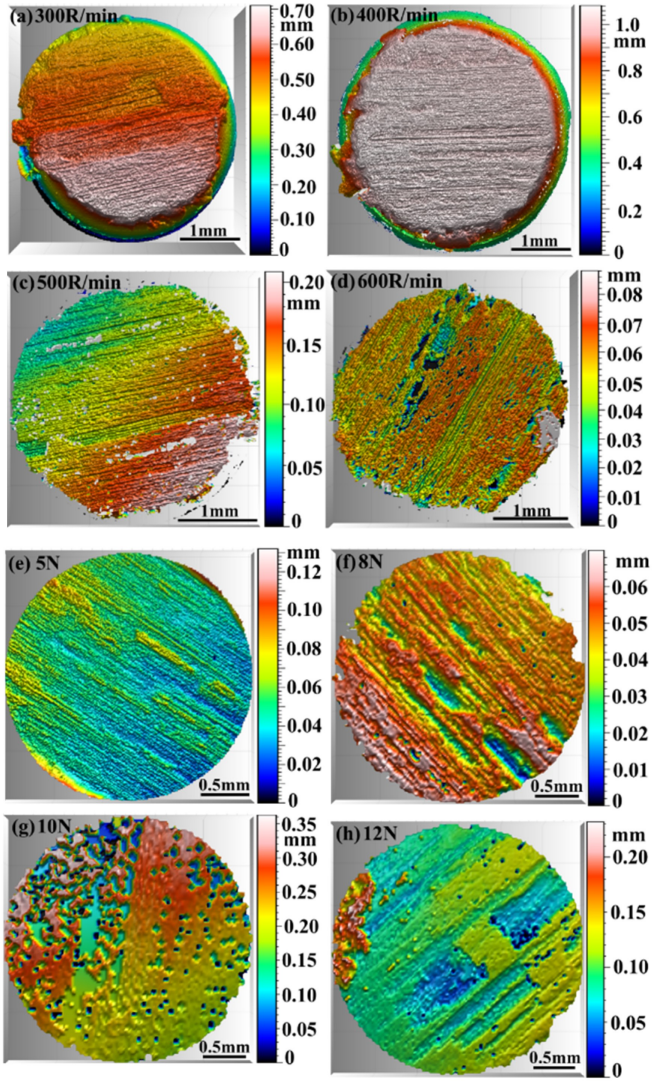

Figure 17. 3D image of wear track of Al ball under 9.8 N at 300 R/min (a); 400 R/min (b); 500 R/min (c); 600 R/min (d); under 5 N (e); 8 N (f); 10 N (g); 12 N (h) at 400 R/min.

4. Discussion the stability of Ti_3SiC_2 under HPHT

Figure 18 illustrates the pressure–temperature stability of Ti_3SiC_2 in the presence of 80 wt% diamond. The dashed line represents the stability limit of Ti_3SiC_2, beyond which decomposition into TiC occurs with increasing temperature and pressure [23]. Ti_3SiC_2 was synthesized from an mixture of Ti/Si/Al/C under a high pressure of 2 GPa and 1300 °C for 60 min [24]. In the Ti_3SiC_2-cBN system, the cBN hard phase can also enhance the stability of Ti_3SiC_2 under high temperature and pressure conditions [6]. Ti_3SiC_2 maintains stability up to ~5.5 GPa and 1250 °C when combined with high diamond content, whereas the narrower stability field of pure Ti_3SiC_2 without reinforcement. This suggests that diamond effectively partitions the Ti_3SiC_2 matrix into isolated domains, suppressing the thermal diffusion of the Si atomic layers and delaying decomposition [14], a mechanism similar to the stability enhancement reported for Ti_3AlC_2-

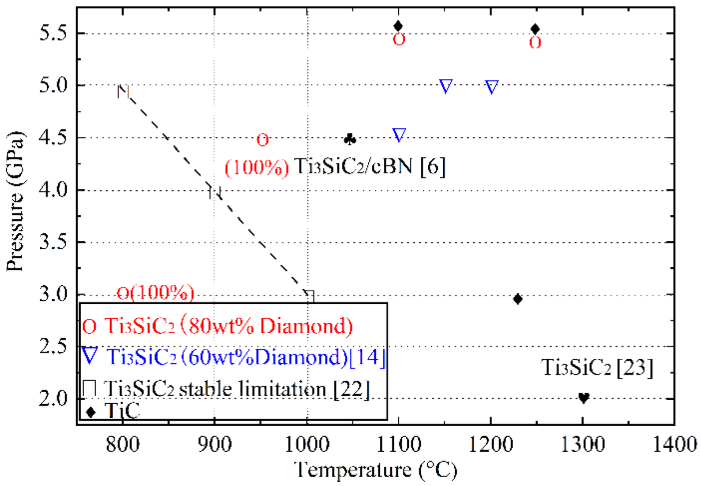

Figure 18. Comparison of stable area of Ti_3SiC_2 and Ti_3SiC_2-based composites.

and Ti_2AlC-based composites with hard phases such as cBN [7, 25-28]or TiC [11].

Compared with Ti_3SiC_2 alone, $Ti_3Si_{0.8}Al_{0.2}C_2$ solid solutions achieve stability through Al–Si substitution, which broadens the single-phase formation and improves oxidation resistance [14, 29]. In contrast, the diamond reinforcement observed here provides an indirect stabilization route by physically confining the layered Ti_3SiC_2 structure. Thus, while $Ti_3(Al,Si)C_2$ relies on chemical substitution to suppress layer diffusion, the 80 wt% diamond composite achieves a comparable effect through microstructural confinement. The result is an enlarged high-pressure, high-temperature stability region, demonstrating that diamond content is a critical factor in maintaining the structural integrity of Ti_3SiC_2 under extreme sintering conditions.

5. Conclusions

The XRD results demonstrate that Ti_3SiC_2 retains structural stability with diamond up to ~1100 °C under 4.5 GPa, while further increases in temperature and pressure induce decomposition into TiC and diamond-derived phases. SEM analysis reveals that increasing sintering pressure and power enhances densification and interfacial bonding, while maintaining uniform diamond distribution within the Ti_3SiC_2 matrix. The Dia.-TSC composites exhibit low COF (0.1–0.22) and stable wear behavior against agate, with abrasive wear dominating and oxide film formation contributing to improved interfacial stability under higher loads and speeds. The Dia.-TSC composites show moderate COF (0.26–0.38) and uniform wear against POM, with grain boundary exfoliation and a transition from abrasive to adhesive wear governing the tribological response under increasing speed and load. The Dia.-TSC composites exhibit relatively high and load-dependent COF (0.47–0.78) against PP, with fatigue wear evolving into abrasive wear at higher speeds and loads due to diamond grain exfoliation and debris embedding. Dia.-TSC composites against Al exhibit load- and speed-dependent friction (0.49–0.93) with adhesive, plowing, and cutting wear dominated by Al debris adhesion and transfer. The incorporation of 80 wt% diamond significantly enlarges the high-pressure, high-temperature stability window of Ti_3SiC_2 by confining Si-layer diffusion and delaying decomposition into TiC.

Funding: This research was funded by the Natural Science Foundation of Henan Province, grant number 242300421464 and 252300420062; the Doctoral Special Fund Project of Nanyang Normal University, grant numbers 2024ZX025; and the Cultivation Project of the National Natural Science Foundation of Nanyang Normal University, grant numbers 2024PY023 and 2023PY011.

Conflict of Interest: The authors declare no potential conflicts of interest with respect to the research, authorship, and/or publication of this article.

References

[1] Ji Huanli, Liang Yuxin, Jiang Ziling, Li Zhihong, Zhu Yumei. Controllable HTHP sintering and property of cBN/diamond composites containing Ti_3SiC_2. Ceramics International, 46(9), 13807-12. 2020. https://doi.org/10.1016/j.ceramint.2020.02.170

[2] Lv Xiaoxin, Jian Qi, Li Zhihong, Sun Kun, Ji Huanli, Zhu Yumei. Effect of controllable decomposition of MAX phase (Ti_3SiC_2) on mechanical properties of rapidly sintered polycrystalline diamond by HPHT. Ceramics International, 45(13), 16564-8. 2019. https://doi.org/10.1016/j.ceramint.2019.05.193

[3] Jaworska Lucyna. The Influence of the binder phase on the properties of high-pressure sintered diamond polycrystals or composites for cutting tool applications. Materials, 18(3), 634. 2025. https://doi.org/10.3390/ma18030634

[4] Laurindo Quezia Manuela Gonçalves, Rosa Joice Medeiros Borges, da Silva Guimarães Renan, Xing Yutao, Franceschini Filho Dante Ferreira, de Andrade Mônica Calixto, Teixeira Silvio Rainho, Fortulan Carlos Alberto, Lima Ludiane Silva, de Carvalho Eduardo Atem. Processing a new diamond composite by high pressure and high temperature with improved thermostability using Mo as a binder. Ceramics International, 50(21), 42256-63. 2024. https://doi.org/10.1016/j.ceramint.2024.08.071

[5] Xiao Changjiang, Zheng Haoyu, Tang Lihui. Effects of composite binder and sintering temperature on the microstructure, properties and reaction mechanism of polycrystalline diamond. Materials Today Communications, 41(110931. 2024. https://doi.org/10.1016/j.mtcomm.2024.110931

[6] Li Zhengyang, Zhou Aiguo, Li Liang, Wang Libo, Hu Meihua, Li Shangsheng, Gupta Surojit. Synthesis and characterization of novel Ti_3SiC_2–cBN composites. Diamond and related materials, 43(29-33. 2014. https://doi.org/10.1016/j.diamond.2014.01.008

[7] Li Liang, Zhou Aiguo, Wang Libo, Li Shangsheng, Wu Dongxu, Yan Chengqi. In situ synthesis of cBN–Ti_3AlC_2 composites by high-pressure and high-temperature technology. Diamond and related materials, 29(8-12. 2012. https://doi.org/10.1016/j.diamond.2012.07.002

[8] Jaworska L, Stobierski L, Twardowska A, Królicka D. Preparation of materials based on Ti–Si–C system using high temperature–high pressure method. Journal of Materials Processing Technology, 162(184-9. 2005. https://doi.org/10.1016/j.jmatprotec.2005.02.172

[9] Jaworska L, Szutkowska M, Morgiel J, Stobierski L, Lis J. Ti_3SiC_2 as a bonding phase in diamond composites. Journal of Materials Science Letters, 20(19), 1783-6. 2001. https://doi.org/10.1023/A:1012535100330

[10] Jaworska L. Diamond composites with TiC, SiC and Ti_3SiC_2 bonding phase. International Journal of High Pressure Research, 22(3-4), 531-3. 2002. https://doi.org/10.1080/08957950212434

[11] Li Liang, Chen Yuqi. The Influence of Sintering Pressure on the Preparation, Friction Properties, and Magnetic Properties of Ti_2AlC-TiC and Ti_3AlC_2-TiC Composites Under High-Pressure and High-Temperature. Advances in Materials Science and Engineering, 2022(1), 9108736. 2022. https://doi.org/10.1155/2022/9108736

[12] Han Huali, Qian Zhiyuan, Meng Fanming, Cui Zhongtao. Tribological performances of graphite–MoS_2 coating at various high temperatures. Proceedings of the Institution of Mechanical Engineers, Part J: Journal of Engineering Tribology, 233(12), 1888-902. 2019. https://doi.org/10.1177/1350650119851688

[13] Liao Yan-ling, Zhang Feng-lin, Pan Xiao-yi, Li Kai-jiang, Zhou Yu-mei, Wu Shang-hua. A comparative study on tribological behavior of Al_2O_3, AlN, Si_3N_4 and ZrO_2 ceramics sliding against polycrystalline diamond ball. Wear, 530(205067. 2023. https://doi.org/10.1016/j.wear.2023.205067

[14] Yuqi Chen, Liang Li, Shibang Ma, Chao Li, Songhao Zheng, Wucheng Lv, Libo Wang, Aiguo Zhou, Xing Wang. Preparation of $Ti_3Si_{0.8}Al_{0.2}C_2$ bonded diamond composites and their friction properties coupled with different counterfaces. Advances in Materials Science and Engineering, 2023(1), 1740345. 2023. https://doi.org/10.1155/2023/1740345

[15] Li Xu, Dai Wei, Wang Qimin, Liang Yunpeng, Wu Zhengtao. Diamond-like/graphite-like carbon composite films deposited by high-power impulse magnetron sputtering. Diamond and Related Materials, 106(107818. 2020. https://doi.org/10.1016/j.diamond.2020.107818

[16] Ta Huong TT, Tran Nam V, Righi Maria Clelia. Atomistic wear mechanisms in diamond: effects of surface orientation, stress, and interaction with adsorbed molecules. Langmuir, 39(40), 14396-403. 2023. https://doi.org/10.1021/acs.langmuir.3c01800

[17] Roy Amit, Patel Payank, Sharifi Navid, Chromik Richard R, Stoyanov Pantcho, Moreau Christian. Binary and ternary lubricious oxides for high temperature tribological applications: A review. Results in Surfaces and Interfaces, 11,100117. 2023. https://doi.org/10.1016/j.rsurfi.2023.100117

[18] Kurkcu Pinar, Andena Luca, Pavan Andrea. An experimental investigation of the scratch behaviour of polymers–2: Influence of hard or soft fillers. Wear, 317(1-2), 277-90. 2014. https://doi.org/10.1016/j.wear.2014.03.011

[19] Chen Yuqi, Li Liang, Han Ming, Sun Chaofan, Li Jin. Sintering and tribological properties of Ti_3SiC_2-$TiSi_x$ composite sintered by high-pressure high-temperature technology. Materials, 17(19), 4866. 2024. https://doi.org/10.3390/ma17194866

[20] Ye Jiaxin, Burris David L, Xie Ting. A review of transfer films and their role in ultra-low-wear sliding of polymers. Lubricants, 4(1), 4. 2016. https://doi.org/10.3390/lubricants4010004

[21] Kan Wen Hao, Chang Li. The mechanisms behind the tribological behaviour of polymer matrix composites reinforced with TiO_2 nanoparticles. Wear, 474 (203754. 2021. https://doi.org/10.1016/j.wear.2021.203754

[22] Panin Sergey V, Alexenko Vladislav O, Buslovich Dmitry G. High performance polymer composites: A role of transfer films in ensuring tribological properties—A review. Polymers, 14(5), 975. 2022. https://doi.org/10.3390/polym14050975

[23] Qin Jiaqian, He Duanwei. Phase stability of Ti_3SiC_2 at high pressure and high temperature. Ceramics International, 39(8), 9361-7. 2013. https://doi.org/10.1016/j.ceramint.2013.04.111

[24] Li Xuhai, Xu Liang, Chen Qingyun, Cao Xiuxia, Liu Lixin, Wang Yuan, Zhang Haibin, Meng Chuanmin, Wu Qiang. Investigation of formation mechanism of Ti_3SiC_2 by high pressure and high-temperature synthesis. High Pressure Research, 38(4), 440-7. 2018. https://doi.org/10.1080/08957959.2018.1501045

[25] Rampai Tokoloho, Sigalas Iakovos, Whitefield David. Utilization of moderate pressure and elevated temperatures in the optimization of Ti_2AlC-cBN composites using SPS technique. International Journal of Ceramic Engineering & Science, 3(2), 60-76. 2021. https://doi.org/10.1002/ces2.10080

[26] Yue Zhenming, Yang Limin, Gong Jianhong, Gao Jun. Synthesis and comparison of two cBN composites with starting ternary carbide binders. Journal of Materials Engineering and Performance,

27(5), 2124-30. 2018. https://doi.org/10.1007/s11665-017-2876-3

[27] Yang Limin, Gong Jianhong, Yue Zhenming, Chu Xingrong. Preparation and characterization of cBN-based composites from cBN-Ti_3AlC_2 mixtures. Diamond and Related Materials, 66(183-7. 2016. https://doi.org/10.1016/j.diamond.2016.05.003

[28] Jiang Ziling, Jian Qi, Han Yang, Zhu Yumei, Li Zhihong. Performance evaluation of cBN-Ti_3AlC_2–Al composites fabricated by HTHP method. Ceramics International, 46(15), 24449-53. 2020. https://doi.org/10.1016/j.ceramint.2020.06.228

[29] Wei Yulin, Li Xiaoyue, Yang Chenhao, Liu Junxiong, Peng Ping, Liu Min. Enhanced He irradiation-resistance of M/A-site two-component MAX phase revealed via defect evolution. Journal of Nuclear Materials, 606(155615. 2025. https://doi.org/10.1016/j.jnucmat.2025.155615